Wheel-speed based Driving Force Control for On-board Motor Electric Vehicles with Absolute Stability Analysis and HIL Evaluation

Yuki Hosomi, Binh-Minh Nguyen, Hiroshi Fujimoto
The University of Tokyo
5-1-5, Kashiwanoha, Kashiwa, Chiba, 277-8561, Japan
Corresponding author's e-mail: fujimoto@k.u-tokyo.ac.jp

Hiroaki Ikeda, Tatsuro Nohara
Komatsu Ltd.
3-25-1, Shinomiya, Hiratsuka, Kanagawa, 254-8555, Japan
tatsurou_nohara@global.komatsu

***Abstract*—Driving force control (DFC) has been well-developed for in-wheel-motor electric vehicles (IWM-EVs). However, due to the powertrain complexity, DFC for on-board motor electric vehicles (OBM-EVs) is still an open challenge, especially in system configuration and stability analysis. To address these issues, this paper proposes (i) a novel cascade two-degree-of-freedom DFC for OBM-EVs and (ii) an absolute stability analysis of the overall system with respect to the maximum allowable wheel speed, which depends on the driving situation. In the outer layer, a feedback-feedforward reaction force controller directly generates the wheel speed references. In the inner layer, a feedback-feedforward speed controller generates the motor torque. By utilizing a real IWM-EV, a hardware-in-the-loop (HIL) system is developed to imitate the OBM-EV properly. HIL results show that the proposed stability analysis can effectively predict the system behavior. The proposed system successfully improves the DFC performances with quick response, less vibration, and accurate tracking.**

***Index Terms*—electric vehicle, absolute stability, driving force control, driving force observer, on-board motor.**

I. Introduction

Electric vehicle technology is advancing [1], and electrification is progressing not only in passenger vehicles but also in construction machinery such as dump trucks. Behind the spread of EVs, various energy optimization studies have been conducted to achieve the range extension of electric vehicles (EVs) [2], [3]. Furthermore, motors are superior to internal combustion engines in terms of motion control because they have a much faster torque response and an accurate measurement of the actual torque. Thanks to these merits, many advanced motion controls have been developed, such as chassis control [4], yaw moment control [5], [6], and vibration suppression [7].

The focus of this paper is a safe and comfortable traction control for EVs. To achieve this goal, several controllers have been developed, mainly for in-wheel-motor electric vehicles (IWM-EVs). There are three types of controllers, such as anti-slip control (ASC) [8], [9], slip ratio control (SRC) [10], [11], and driving force control (DFC) [12]. ASC is a disturbance observer-based controller that regulates the excessive slip ratio, thus it is impossible for ASC to utilize driving force reference directly. Similarly, the reference of SRC is the slip ratio. Therefore, ASC is hard to combine with other higher-layer motion controllers. On the other hand, DFC can accurately track the driving force with the desired value by utilizing a cascade configuration with force control in the outer layer and motor speed control in the inner layer.

However, the family of EVs includes not only IWM-EVs but also on-board motor electric vehicles (OBM-EVs), which have many promising applications such as buses and trucks. The drivetrain from the motor to the tires of OBM-EVs is more complex than that of IWM-EVs. DFC for OBM-EVs was preliminarily studied in [13] and [14], which were merely copies of IWM-EV DFC. To develop the OBM-EVs version of DFC, we recently proposed a higher-order motor speed controller and a driving force observer (DFO) that simultaneously estimates the viscous friction coefficient [15]. However, the study [15] still faces two essential issues. (i) From a system configuration point of view, the DFC [15] is quite complex and not practical, as it requires the accurate measurement of vehicle chassis velocity. On the other hand, [15] did not consider the design and integration of the feedforward control signal with the feedback control signal. (ii) From a system analysis point of view, no theoretical approach exists to analyze the overall DFC system for OBM-EV. Although absolute stability has been considered for the first time in [16], it is an IWM-EV version.

With respect to the above discussion, this paper proposes a novel DFC strategy for OBM-EVs. The proposed control system has a two-degree-of-freedom cascade configuration, which means both the outer layer and inner layer consist of the feedback and feedforward controllers. Notably, the outer layer's reaction force control directly outputs the wheel speed reference. The chassis velocity is only used to calculate the upper bound for the wheel speed reference limiter. In addition, this paper presents a new feedforward force controller for the outer layer, which can eliminate the steady-state error that is the remaining problem of the previous method [16]. Furthermore, an absolute stability condition has been established to address the wheel speed limiter, which must be implemented in the system for the purpose of slip prevention. The proposed strategy was validated using a hardware-in-the-loop (HIL)

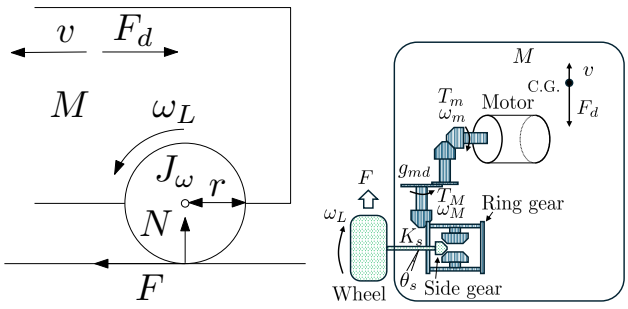

(a) Vehicle model. (b) Drivetrain model.

Fig. 1. Single-wheel OBM-EV with a differential gear and drive shafts.

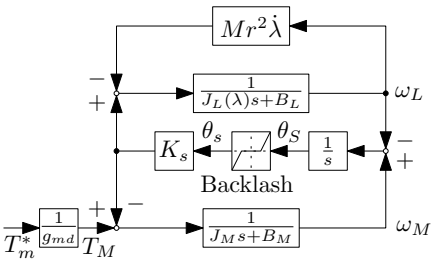

Fig. 2. Drivetrain block diagram.

system, which was originally developed by our research group by using a real IWM-EV [15]. Test results clarify that the proposed system can attain good tracking performance without overshooting and reduce vibration. Especially, the absolute stability analysis allows us to do a graphical test, which shows a practical approach to predict and tune the behavior of the overall system.

II. Modeling

A. Vehicle dynamics

For DFC design, this paper considers the longitudinal motion of the single-wheel vehicle model depicted in Fig. 1(a). The equations of vehicle longitudinal motion are expressed as

$$M\frac{dv}{dt} = F - F_d, \tag{1}$$

$$F_d = \mu_{\mathrm{r}} Mg + b|v| + \frac{1}{2}\rho C_d A v^2, \tag{2}$$

where M, v, F_d, μ_{r}, b, and $\frac{1}{2}\rho C_d A$ are the vehicle mass, vehicle chassis speed, resistance force of road friction and air resistance, rolling resistance coefficient, viscous resistance coefficient, and air resistance coefficient, respectively. The equation of driving force is $F = \mu(\lambda)N$ which is the product of the vehicle load N and the friction coefficient of the road surface μ, and the friction coefficient is determined by the magic formula proposed by Pacejka with slip ratio λ as a variable [17]. λ is defined as

$$\lambda = \frac{r\omega_L - v}{\max(r\omega_L, v, \epsilon)}, \tag{3}$$

where ϵ, r, and ω_L are a small positive value preventing zero division, the wheel radius, and the wheel speed. To match the definition for both acceleration and deceleration, controllers use a variable y instead of λ [15]. The definition of y is expressed as

$$y = \frac{v_\omega}{v} - 1. \tag{4}$$

As for the OBM drive systems, the motor connects to the tires via a reduction gear and a differential gear as shown in Fig. 1(b). By using the combinations of torque and angular speed of both the motor (T_m, ω_m) and the ring gear (T_M, ω_M), the equations of reduction gear are summarized as

$$\omega_M = g_{md}\omega_m, \quad T_M = \frac{T_m}{g_{md}}, \tag{5}$$

where g_{md} is the gear ratio. The differential gear distributes the output torque of the reduction gear to the left and right side gears and transmits it to the tires through the drive shafts. Besides, the rotational motion of the drive and load side of the drivetrain system are expressed as follows,

$$J_M\dot{\omega}_M = T_M - B_M\omega_M - K_s\theta_s, \tag{6}$$

$$J_{L0}\dot{\omega}_L = K_s\theta_s - B_L\omega_L - rF, \tag{7}$$

where K_s is the driveshaft rigidity, and $J_M = J_m/g_{md}^2 + J_{\mathrm{input}} + J_{\mathrm{ring}} + J_{\mathrm{pinion}}$, $J_{L0} = J_{side} + J_{drive} + J_\omega$, B_M, and B_L are the sum of inertias of components and viscous friction coefficients of both the drive side and load side, respectively. Lastly, Equations (8) and (9) represent the backlash of the differential gear.

$$\theta_s = \begin{cases} \theta_S - \theta_b & (\theta_S > \theta_b) \\ 0 & (-\theta_b \le \theta_S \le \theta_b) \\ \theta_S + \theta_b & (\theta_S < -\theta_b), \end{cases} \tag{8}$$

$$\theta_S = \int (\omega_M - \omega_L)dt, \tag{9}$$

where θ_b is the boundary value of the deadband.

B. Drivetrain model

To define a two-inertia drivetrain model, the resistance force F_d is considered as a disturbance term. Based on (1) and (3), the driving force can be expressed with the slip ratio λ instead of vehicle chassis speed v as $F = M\dot{v} = Mr^2(1-\lambda)\dot{\omega}_L + Mr^2\dot{\lambda}\omega$. Combining this equation and (7), the rotational motion of the wheel is expressed as

$$J_L(\lambda)\dot{\omega}_L = K_s\theta_s - B_L\omega_L - Mr^2\dot{\lambda}\omega_L, \tag{10}$$

$$J_L(\lambda) = J_{L0} + Mr^2(1-\lambda). \tag{11}$$

Due to (6), (8), (9), and (10), the drivetrain can be modeled as a two-inertia system, and the block diagram of the drivetrain plant is shown in Fig. 2. By assuming a constant slip ratio λ_n and ignoring the effect of backlash, the transfer functions from

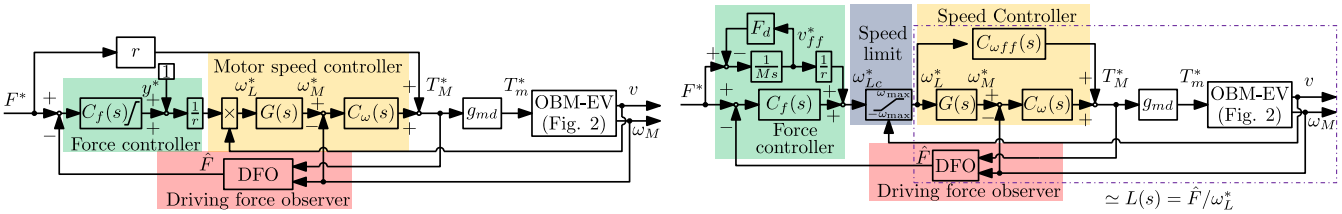

(a) Conventional DFC. (b) Proposed DFC.

Fig. 3. Comparison of overall driving force controller.

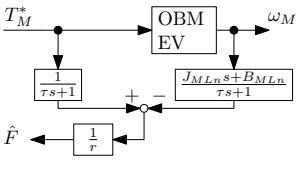

Fig. 4. DFO configuration.

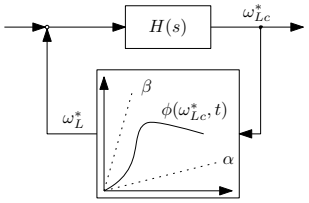

Fig. 5. Equivalent of the overall system for stability analysis.

the motor torque to the motor speed $P_{Mn}(s)$ and wheel speed $P_{Ln}(s)$ are obtained as

$$P_{Mn}(s) = \frac{\omega_M}{T_M} = \frac{J_L(\lambda_n)s^2 + B_L s + K_s}{a_{n3}s^3 + a_{n2}s^2 + a_{n1}s + a_0} \tag{12}$$

$$P_{Ln}(s) = \frac{\omega_L}{T_M} = \frac{K_s}{a_{n3}s^3 + a_{n2}s^2 + a_{n1}s + a_0} \tag{13}$$

where a_{n3}, a_{n2}, a_{n1}, a_0 are defined as $a_{n3} = J_M J_L(\lambda_n)$, $a_{2,n} = J_L(\lambda_n)B_M + J_M B_L$, $a_{n1} = B_M B_L + J_M K_s + J_L(\lambda_n)K_s$, $a_0 = (B_M + B_L)K_s$.

III. Cascade Driving Force Control

A. Outline of the proposal

Block diagrams of overall DFC systems are shown in Figs. 3. The output of the force controller is changed to wheel speed in the proposed method, which eliminates the product of vehicle speed. Feedforward controllers are introduced for each of the force and speed controllers. The proposed DFC has four main components, Speed controller, wheel speed limiter, DFO, and reaction force controller as shown in Fig. 3(b). It is the cascade configuration of the inner layer speed controller and outer layer force controller. The feedback signal of the driving force is generated by DFO.

The wheel speed limiter is defined as

$$\omega_{\max} = (1 + y_{\max})\frac{v}{r}, \tag{14}$$

where $y_{\max}$ is the maximum allowable slip ratio to prevent the wheel slip. Considering the reduction gear, the output torque T_M^* of the speed controller is multiplied by gear ratio g_{md} to calculate T_m^*. Speed controller, DFO, and reaction force controller will be designed in the following subsections.

B. Motor speed control

The motor speed controller consists of a motor speed feedback controller and a wheel speed-based feedforward controller. As the motor speed feedback controller, a proportional-integral-differential (PID) controller and phase lead compensator are used with the reference generator $G_{L\to M}(s)$ [15], and they are defined as

$$C_w = \left(k_p + \frac{k_i}{s} + \frac{k_d s}{\tau_d s + 1}\right)\left(\frac{\tau_1 s + 1}{\tau_2 s + 1}\right), \tag{15}$$

$$G_{L\to M}(s) = Q(s)P_{Ln}^{-1}(s)P_{Mn}(s), \tag{16}$$

where $Q(s) = 1/(\tau_Q s + 1)^3$ is a third-order low-pass filter to make $G_{L\to M}(s)$ proper, and τ_Q is the time constant of the filter.

As the wheel speed-based feed-forward controller, the transformation from ω_L^* to T_M^* can be derived as

$$C_{\omega ff} = Q(s)P_{Ln}^{-1}(s). \tag{17}$$

C. Driving force observer

As for the load side force observer, there are some attempts to establish a state space observer using four variables w_M, w_L, θ_s, and F [18]. However, the resolution of the load side sensor for ω_L is not as high as the drive side motor speed sensor for ω_M. Thus, this paper formulates DFO as a one-inertia drivetrain with the assumption that ω_M is almost equal to ω_L. Accordingly, by summarizing (6) and (7), we have

$$J_{MLn}\dot{\omega}_M = -B_{MLn}\omega_M - rF + T_M, \tag{18}$$

where $J_{MLn} = J_M + J_{L0}$ and $B_{MLn} = B_M + B_L$. Using (18) and the first-order low-pass filter with the time constant τ, the driving force can be estimated as shown in Fig. 4.

D. Reaction force controller design with absolute stability

The conventional DFC uses an integral force controller $C_f(s)$. On the contrary, the proposed method uses a proportional-integral (PI) controller which is defined as,

$$C_f(s) = K_{FP} + \frac{K_{FI}}{s} \tag{19}$$

Based on (1), the reaction force feedforward controller can be derived as

$$\omega_{Lff}^* = \frac{1}{rM}\int F^* - F_d dt \tag{20}$$

Equivalent transfer function $H(s) = C_f(s)\hat{F}/\omega_L^*$ is used to evaluate stability analysis as shown Fig. 5. The transfer function from wheel speed reference w_L^* to estimated driving force $\hat{F}$ is calculated as shown in below,

$$\hat{F} = Q_f T_M^* - Q_f(J_{MLn}s + B_{MLn})w_M, \tag{21}$$

$$T_M^* = \frac{C_{\omega ff} + C_\omega G}{1 + C_w P_{Mn}}\omega_L^*, \tag{22}$$

$$w_M = P_{Mn} T_M^*. \tag{23}$$

Using these equations, the transfer function $L(s)$ is defined as,

$$L(s) = \frac{\hat{F}}{\omega_L^*} = Q_f(C_{\omega ff} + C_\omega G)\frac{1 - P_{Mn}(J_{MLn}s + B_{MLn})}{1 + C_w P_{Mn}} \tag{24}$$

From this transfer function, $L(s)$ has a zero at the origin. Thus, the PI controller is not able to eliminate steady-state error for step reference. Thus, the feedforward wheel speed reference ω_{Lff}^* is crucial to reduce steady-state error.

We can analyze the DFC stability using the nominal slip ratio λ_n. The derivative of slip ratio $\dot{\lambda}$ and backlash can be treated as disturbance due to the change of road condition to the system. Using an equation of the feedback connection of $H(s) = L(s, \lambda_n)C_f(s)$, the block diagram of the proposed DFC system can be rewritten as shown in Fig. 5. By the Routh-Hurwitz stability criterion, $H(s)$ is shown to be Hurwitz if the stable poles of the speed controller and the positive gains of the force controller are selected. Then, the absolute stability of the proposed method can be evaluated by the $H(s)$. As presented in [19], the saturation block with the input ω_{Lc}^* and the output ω_L^* can be treated as a time-varying nonlinear gain ϕ which belongs to a specific sector bound $[\alpha, \beta]$, $\alpha \le \phi(\omega_{Lc}^*, t) \le \beta$. As shown in Fig. 6, the wheel speed limit is defined with the upper-bound $\beta = 1$ and lower-bound α. The value of α is selected as greater than 0 and less than 1. As for $\alpha = 1$, there is no limiter, and when $\alpha = 0$, the stability analysis is too conservative to guarantee good tracking performance [16]. Since $H(s)$ is Hurwitz, the following design condition is defined.

- Stability condition: The DFC system is absolutely stable if the Nyquist plot of $H(j\omega)$ does not enter the disk $D(\alpha, \beta)$ defined in Fig. 7

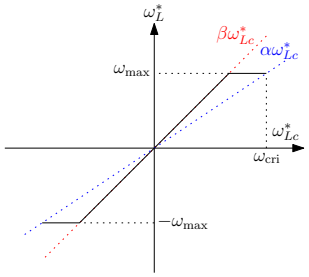

Fig. 6. Wheel speed limiter.

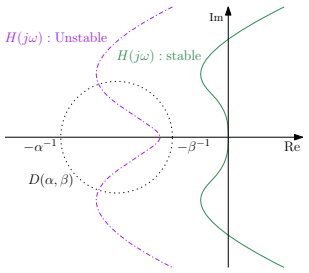

Fig. 7. Circle criterion.

IV. Simulation

A. Simulation setting

Numerical simulations are performed using an OBM-EV. The main parameters of the vehicle are summarized in Table I. Inertias and viscous friction coefficients of the drivetrain are obtained by the frequency domain parameter identification using an actual OBM-EV.

With respect to the speed controller, the high-order speed controller is designed by a two-inertia drivetrain model P_{Mn} when the nominal slip ratio λ_n is 0.05 [15]. We set the parameters as $k_p = 138$, $k_i = 6$, $k_d = 0.6$, $\tau_d = 0.004$, $\tau_1 = 0.005$, $\tau_2 = 0.001$, and $\tau_Q = 0.12$, respectively. The time constant of DFO τ is 0.07, and the nominal slip ratio λ_n is 0.05.

TABLE I
Vehicle Parameters.

Parameter	Value
J_M	$1.55\,\text{kgm}^2$
J_{L0}	$1.24\,\text{kgm}^2$
B_M	$3.1\,\text{Nms/rad}$
B_L	$0\,\text{Nms/rad}$
K_s	$2784\,\text{Nm/rad}$
M	$1300\,\text{kg}$
r	$0.27\,\text{m}$

To select a reasonable value of α, it is determined by $\alpha = \omega_{\max}/\omega_{\text{cri}}$ as shown in Fig. 6. Using λ, we can define $\omega_{\max}, \omega_{\text{cri}}$ as shown below,

$$\omega_{\max} = \frac{1}{1 - \lambda_s}\frac{v}{r}, \quad \omega_{\text{cri}} = \frac{1}{1 - \lambda_{\text{cri}}}\frac{v}{r}, \tag{25}$$

where λ_s and λ_{cri} are the slip limiter $\lambda_s = y_{\max} = 0.05$ and the ciritical slip ratio. Thus, we can select the lower-bound α.

$$\alpha = \frac{\omega_{\max}}{\omega_{\text{cri}}} = \frac{1 - \lambda_{\text{cri}}}{1 - \lambda_s} \tag{26}$$

$\lambda_s = 0.05$, $\lambda_{\text{cri}} = 0.7$. Thus, α is assumed to be almost 0.3. This paper evaluates the stability analysis with the sector bound $[0.3, 1]$.

B. Stability analysis for the simulation vehicle

As for the reaction force PI controller, the proportional gain K_{FP} is set to 0.0001. The three types of integral gains K_{FI} are 0.01, 0.03, and 0.0423. The graphical tests of three controllers by circle criterion are shown in Fig. 8(a). The Nyquist plots of controllers with a large integral gain close to the edge. The controller with $K_{FI} = 0.0423$ is on the edge of absolute stability.

C. Simulation result

Figs. 8(b) and 8(c) show the simulation results of driving force and motor speed. Comparing controllers with K_{FI} of 0.01 and 0.03, which are stable controllers, there is no error in the steady state. The response is better with a larger integral gain. The controller with $K_{FI} = 0.0423$, which reached the edge of the disk in the stability analysis, is found to be unstable

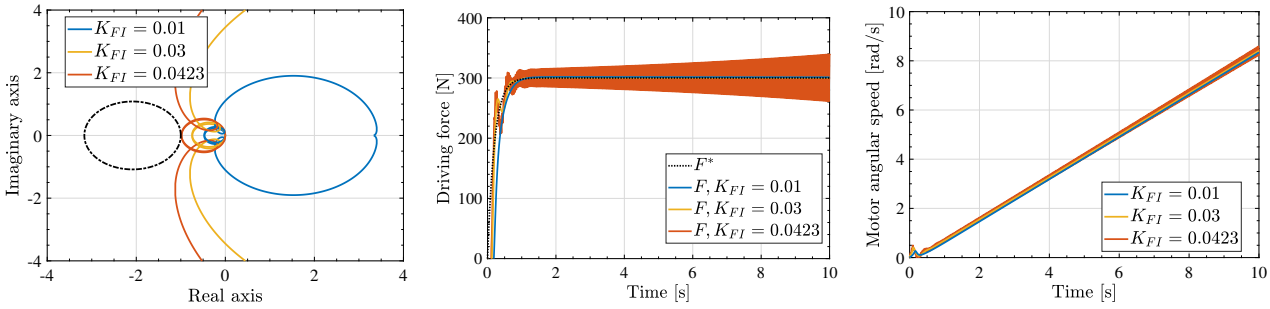

(a) Stability analysis. (b) Driving force. (c) Motor speed.

Fig. 8. Numerical simulations of the proposed stability analysis.

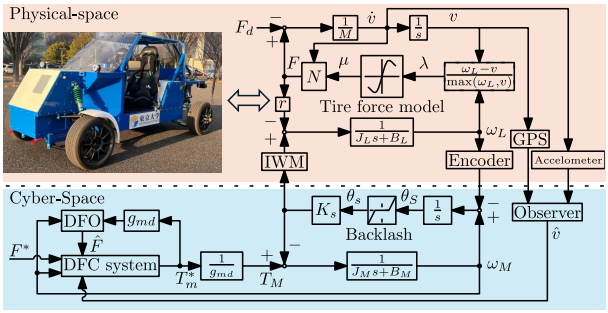

Fig. 9. Hardware-in-the-loop experimental setup.

due to increased oscillations in both motor speed and driving force.

V. Experimental Evaluation

A. Real-vehicle based HIL experimental setup

HIL experiment validates the stability analysis and evaluates the proposed DFC system. As shown in Fig. 9, the load side of the two-inertia drivetrain is the real rear-left-IWM of the experimental vehicle FPEV5 [15]. FPEV5 has a dSPACE DS1007 processor board as the on-board controller that runs the DFC system and real-time simulation from the motor to the differential. The vehicle chassis speed is estimated by GPS speed and acceleration whose sampling periods are 1 Hz and 100 Hz, respectively.

B. Stability analysis for the experimental vehicle

The reaction force controller gain are $K_{FP} = 0.001$, and the value of K_{FI} is 0.01, 0.0175, and 0.02. The graphical tests of three controllers by circle criterion are shown in Fig. 10(a). The high gain reaction force controller of $K_{FI} = 0.02$ enters the disk. The smaller gain reaction force controller $K_{FI} = 0.0175$ is the edge of the disk. Finally, the controller $K_{FI} = 0.01$ is the stable controller.

C. Experimental result

Figs. 10(b) and 10(c) show the HIL experimental results. When the controller gain is $K_{FI} = 0.01$, the controller is stable. On the other hand, when the controllers are $K_{FI} = 0.0175$ and $K_{FI} = 0.02$ the oscillation occurs, and the controller of $K_{FI} = 0.02$ is unstable. The results match the stability analysis as shown in Fig. 10(a) and verify the proposed method.

We also compare the proposed DFC (Prop.) with the traditional DFC (Conv.). The same motor speed controller as in the proposed method is used. The gain of the reaction force integral controller of conventional DFC is $K_{FI} = 0.002$, which is determined by the parameter tuning in the experiments. The HIL experimental results are shown in Figs. 11(a) and 11(b). Since the reaction force controller of the proposed method is a PI and that of the conventional method is an I controller, the response of the proposed DFC is quicker than that of the conventional DFC. In addition, the feedforward controller improves DFC response. Especially in the proposed DFC, the wheel speed-based feedforward force controller eliminates the steady-state error. Even though vibration around 1 Hz caused by the vehicle chassis speed estimation is observed in the conventional method, it disappears in the proposed method. As a result, the root-mean-square-error (RMSE) values between F^* and $\hat{F}$ show that the proposed method reduces the tracking error by 22.9 % in comparison with the conventional method.

VI. Conclusion

We propose a novel DFC system for OBM-EVs which enables us to analyze the stability by circle criterion. The output of the novel reaction force controller is wheel speed. Due to this reaction force controller, the proposed DFC does not need the product of vehicle chassis speed and the slip ratio and is a linear system that is easy to stability analysis. Moreover, to eliminate the steady-state error, we introduce the reaction force feedforward controller, which is easy to implement. HIL experiments show that the circle criterion can evaluate the stability of the DFC system properly. The proposed DFC system for OBM-EVs can reduce the tracking error. The above methods facilitate parameter tuning of the driving force controller. It reduces the time required for parameter tuning by experimentation, which has been conventionally conducted. We would plan to install the proposed DFC system to the real OBM-EVs. In addition, we verify that the system can be applied to electric dump trucks, including off-road driving.

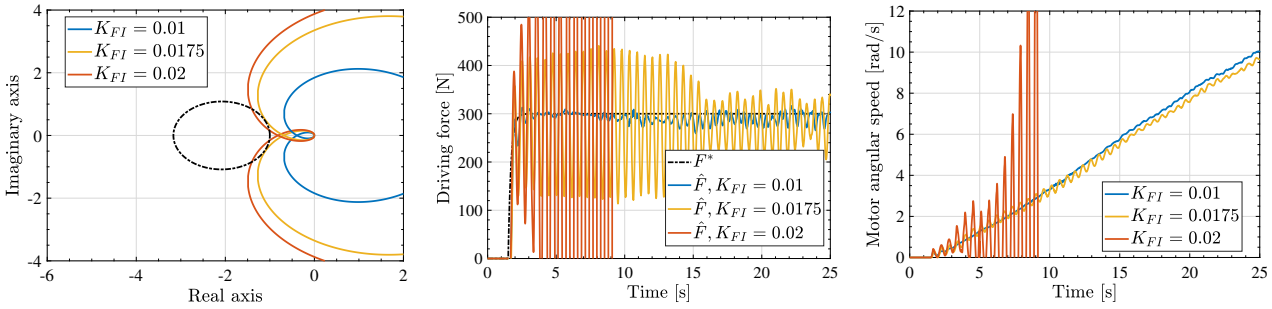

(a) Stability analysis. (b) Driving force. (c) Motor speed.

Fig. 10. HIL experimental evaluation of the proposed stability analysis.

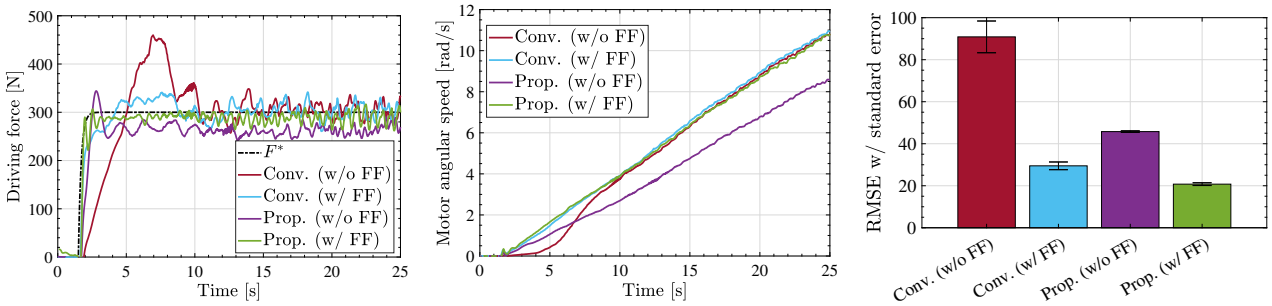

(a) Driving force. (b) Motor speed. (c) Tracking error.

Fig. 11. HIL experimental comparison between conventional and proposed DFC.

REFERENCES

[1] S. Oki and Y. Sato, "Nissan leaf and e-power: Evolution of motors and inverters," *IEEJ Journal of Industry Applications*, vol. 13, no. 1, pp. 8–16, 2024.

[2] Y. Hosomi, B.-M. Nguyen, S. Nagai, and H. Fujimoto, "Learning-based distributed approach to energy-optimized speed trajectory for electric vehicles at multiple signalized intersections," in *IECON 2023- 49th Annual Conference of the IEEE Industrial Electronics Society*, 2023, pp. 1–6.

[3] A. Lotfy, H. Chaoui, M. Kandidayeni, and L. Boulon, "Enhancing energy management strategy for battery electric vehicles: Incorporating cell balancing and multi-agent twin delayed deep deterministic policy gradient architecture," *IEEE Transactions on Vehicular Technology*, pp. 1–16, 2024.

[4] Z. Wang, X. Ding, and L. Zhang, "Chassis coordinated control for full x-by-wire four-wheel-independent-drive electric vehicles," *IEEE Transactions on Vehicular Technology*, vol. 72, no. 4, pp. 4394–4410, 2023.

[5] L. Cai, Z. Liao, S. Wei, and J. Li, "Novel direct yaw moment control of multi-wheel hub motor driven vehicles for improving mobility and stability," *IEEE Transactions on Industry Applications*, vol. 59, no. 1, pp. 591–600, 2023.

[6] A.-T. Nguyen, B.-M. Nguyen, T. Vo-Duy, and M. C. Ta, "Steering vector control for lateral force distribution of electric vehicles," in *2022 IEEE Vehicle Power and Propulsion Conference (VPPC)*, 2022, pp. 1–6.

[7] H. Fuse, H. Fujimoto, K. Sawase, N. Takahashi, R. Takahashi, Y. Okamura, and R. Koga, "Derivation of dynamic model of two-input-two-output torque difference amplification motor drive system and independent left-and-right wheel control with decoupling compensator," *IEEJ Journal of Industry Applications*, vol. 11, no. 3, pp. 427–436, 2022.

[8] J.-K. Lee, J.-W. Kim, and B.-g. Park, "Fast anti-slip traction control for electric vehicles based on direct torque control with load torque observer of traction motor," in *2021 IEEE Transportation Electrification Conference & Expo (ITEC)*, 2021, pp. 321–326.

[9] B.-M. Nguyen, J. P. F. Trovao, M. C. Ta, and M. Kawanishi, "Longitudinal motion control of electric vehicles: Glocal model and design using passivity," *IEEE Vehicular Technology Magazine*, vol. 16, no. 3, pp. 75–86, 2021.

[10] H. Guo, R. Yu, X. Bai, and H. Chen, "Vehicle traction control based on optimal slip using sliding mode controller," in *Proceedings of the 33rd Chinese Control Conference*, 2014, pp. 251–256.

[11] N. T. Nguyen, M. C. Ta, T. Vo-Duy, and V. Ivanov, "Enhanced fuzzy-mfc-based traction control system for electric vehicles," in *2023 IEEE Vehicle Power and Propulsion Conference (VPPC)*, 2023, pp. 01–06.

[12] H. Fujimoto, J. Amada, and K. Maeda, "Review of traction and braking control for electric vehicle," in *2012 IEEE Vehicle Power and Propulsion Conference*, 2012, pp. 1292–1299.

[13] H. Sumiya and H. Fujimoto, "Driving force control method using suppression control of driving-shaft vibration for electric vehicle with on-board motor," in *IEEJ Industry Applications Society Conf*, no. 106, 2012 (in Japanese), pp. 115–120.

[14] H. Fujimoto, T. Miyajima, and J. Amada, "Development of electric vehicle with variable drive unit system," in *International Electric Vehicle Technology Conference & Automotive Power Electronics Japan*, vol. 2014, 2014.

[15] Y. Hosomi, , B. M. Nguyen, H. Fujimoto, H. Ikeda, and T. Nohara, "Driving force control for on-board motor electric vehicles with adaptive drivetrain friction and phase stabilization speed controller," in *2024 IEEE/ASME International Conference on Advanced Intelligent Mechatronics (AIM)*, 2024.

[16] T. Ueno, B.-M. Nguyen, and H. Fujimoto, "Driving force control for in-wheel motor electric vehicles with wheel speed limiter and absolute stability analysis," in *IECON 2023- 49th Annual Conference of the IEEE Industrial Electronics Society*, 2023, pp. 1–6.

[17] H. B. Pacejka and E. Bakker, "The magic formula tyre model," *Vehicle system dynamics*, vol. 21, no. S1, pp. 1–18, 1992.

[18] S. Yamada and H. Fujimoto, "Precise external torque estimation for two-inertia system considering modeling errors," in *2018 Annual American Control Conference (ACC)*, 2018, pp. 5238–5243.

[19] H. K. Khalil, *Control of nonlinear systems*. Prentice Hall, New York, NY, 2002.